



Simulations of fusion edge plasmas by linear plasma devices: physics and plasma–material interactions

In Je Kang^{1,2} · Min-Keun Bae¹ · In Sun Park¹ · Hyun-Jong Woo³ · Taihyeop Lho² · Jeong-Sun Ahn¹ · Doo-Hee Chang¹ · Soon-Gook Cho¹ · Geun-Sik Choi¹ · Heung-Gyun Choi¹ · Yong-Sup Choi¹ · Bo-Hyun Chung¹ · Tae Hun Chung⁴ · Jeong-Joon Do¹ · Bon-Cheol Goo¹ · Sung Hoon Hong¹ · Suk-Ho Hong⁵ · Jong-Sik Jeon¹ · Sung-Kiu Joo¹ · Seo Jin Jung¹ · Seok-Won Jung¹ · Young-Dae Jung⁶ · Yong Ho Jung¹ · Kwang-Cheol Ko⁷ · Beom-Sik Kim¹ · Gon-Ho Kim⁸ · Hye-Ran Kim¹ · Heung-Su Kim⁵ · Jin-Hee Kim¹ · Jong-Il Kim¹ · Jae Yong Kim⁹ · Kyung-Cheol Kim¹ · Myung Kyu Kim¹ · Sang-You Kim¹ · Jin-Woo Kim¹ · Yong-Kyun Kim¹⁰ · Gyea Young Kwak¹ · Dong-Han Lee¹ · Heon-Ju Lee¹¹ · Min Ji Lee¹ · Myoung-Jae Lee⁹ · Seung-Hwa Lee¹ · Eun-Kyung Park¹ · Dong Chan Seok¹ · Byoung-Kyu Lee¹ · Seung Jeong Noh¹² · Young-Jun Seo¹ · Yun-Keun Shim¹ · Jong Ho Sun¹ · Byung-Hoon Oh¹ · Cha-Hwan Oh⁸ · Hye Taek Oh¹ · Young-Suk Oh¹ · Sang Joon Park¹ · Hyun Jong You¹ · Hun Suk You¹ · Kyu-Sun Chung¹

Received: 25 August 2021 / Revised: 26 October 2021 / Accepted: 9 November 2021 / Published online: 28 February 2022
© The Korean Physical Society 2022

Abstract

Because a fusion edge plasma contains various atomic and molecular processes, along with various plasma–material interactions (PMIs) for post-mortem analyses, a linear plasma device can simulate divertor and scrape-off layer (SOL) plasmas with DC edge relevant parameters, although it cannot generate a high ion temperature and toroidicity with much less power density compared to toroidal devices. The Divertor Plasma Simulator-2 (DiPS-2), a linear device with an LaB₆ DC cathode, has been used for a few fusion-relevant physics experiments, including edge localized mode (ELM) simulation and edge transport of diffusion and convection. An ELM simulation has been performed by modulating the magnetic field relevant to the pressure modulation of a toroidal device, and the diffusion coefficients of free and bound presheaths have been measured in simulations of divertor or limiter transport. Moreover, the convection of the filament or the bubble expansion to the first wall has also been analyzed. In addition to various atomic and molecular processes in SOL and divertor plasmas, PMIs must be analyzed both on and beneath the surface of the plasma-facing components (PFCs) because of surface modification. Using DiPS-2 and other linear devices along with Korea Superconducting Tokamak Advanced Research (KSTAR), PMIs have been analyzed in terms of the following elements or processes: (1) boronizations, both for dust interactions with the surface chamber (DiSC) and KSTAR device, are analyzed; (2) carbon damage by the dense heat flux of DiPS-2 is experimentally investigated; (3) the density profile of the lithium injection gettering of hydrogen and its transport experiments (LIGHT-1) device is analytically calculated; (4) the effect of nitrogen on the relaxation of the heat flux to the divertor tile is experimentally analyzed; and (5) tungsten as the divertor tile material is analyzed via laser ELM simulations in terms of dust generation and surface modification.

Keywords Linear plasma devices · DiPS-2 · KSTAR · PMI (plasma–material interaction) · ELM (edge localized mode) · Diffusion · Convection

1 Introduction

Plasma–material interactions (PMIs) in fusion devices are key aspects for the success of advanced tokamaks, such as international thermonuclear experimental reactor (ITER) and demonstration fusion power plant (DEMO), in terms of high performance and safe operation [1]; therefore, the physics of edge plasmas and the mutual interactions between

✉ Kyu-Sun Chung
kschung@hanyang.ac.kr

Extended author information available on the last page of the article

materials and plasmas should be clearly understood. Before a commercial reactor can be implemented, the lack of data under high ion fluence and reactor-relevant divertor plasma conditions with neutron damage requires new experimental devices for the development of plasma-facing materials and components.

PMIs should be analyzed by considering the plasma properties in scrape-off layer (SOL) and the divertor (limiter) regions [2–4], material erosion and deposition [5, 6], impurity transport [7], dust production and detection [8–10], and fuel retention [11]. This requires laboratory simulations of PMIs to quantify the long-term effects of plasma-beam irradiation on plasma facing components (PFCs) with duplication of tedious and multiple procedures. For this, linear plasma devices, compared with toroidal devices, have the advantages of versatility and low cost to simulate divertor and SOL plasmas with DC edge relevant parameters while they do not generate a high ion temperature and toroidicity with much less power density either to the divertor or to the first wall. In particular, linear devices can cover a large part of fusion edge plasmas containing various atomic and molecular processes along with PMIs for post-mortem analyses. Linear devices such as PISCES-A [12, 13] and -B [13], NAGDIS-II [14], PSI-2 [15], and Magnum-PSI [16] have been developed to diagnose and understand the magnetized sheath and pre-sheath regions through basic plasma physics experiments and simulations of tokamak edge plasmas. New linear plasma devices have been proposed based on the initial data. (1) MPEX [17] is a superconducting linear plasma device with magnetic fields of up to 2.5 T in the US fusion program. The plasma source is a high-power helicon source (200 kW, 13.56 MHz). Electrons are heated via electron Bernstein waves with microwaves using multiple 70 GHz gyrotrons (up to 600 kW in total). Ions are heated via ion cyclotron heating in the so-called “magnetic beach heating” scheme in the frequency range of 6–9 MHz (up to 400 kW in total). (2) Another device is LEAD, which is a multi-stage, stage-extensible device [18]. Its three-stage vacuum chamber is approximately 3000 mm long, with cross-section diameters of 400, 400, and 900 mm. A flat-type multi-ring antenna helicon source can produce a large-size plasma column with a maximal diameter of 320 mm. Meanwhile, various plasma devices have been developed in Korea for PMI research: (1) edge plasma simulator—DiPS-2 (HYU); (2) plasma diagnostics developments—DiPS, DiPS-2, DiSC (HYU), and PLAMIS-2 (KFE); (3) material testing by plasma—DiPS-2 (HYU), ECR plasma facility (KFE), ECR source (SNU), high-power plasma torch (KFE), and ion beam facility—PIIID (KIST); (4) thermal heat load testing—plasma torch (SNU), e-beam facility (DKU), and segmented plasma torch (JBNU); and (5) dust particle transport and removal—TRed (HYU), where HYU: Hanyang University, KFE: Korea Institute of Fusion Energy, SNU: Seoul

National University, KIST: Korea Institute of Science and Technology, DKU: Dankook University, and JBNU: Jeonbuk National University [19].

As part of the Basic Fusion Research of the Korean Fusion Program, the Fusion Core Research Center (FCRC) program, in addition to the training researchers, has been an important resource for developing diagnostics and physics for the Korea Superconducting Tokamak Advanced Research (KSTAR) and the ITER devices. Hanyang University has been a part or the center of the FCRC for the past decade: Center for Edge Plasma Science (cEps), Dust interaction of Plasmas with Surfaces (DiPS), and Center for interactions of Materials with Plasmas (cimpL). In this paper, we summarize the research on simulations of fusion edge plasmas using linear plasma devices in terms of physics and plasma–material interactions. The following are discussed: (1) edge localized mode (ELM) simulation in the DiPS-2, and (2) transport simulation in the DiPS-2 concerning Bohm-type diffusion and convection as a filament toward the first wall, by comparing the results for the DiPS-2 and those for the KSTAR. In particular, for the ELM simulations in terms of transient heat fluxes, ELM simulations using (1) laser irradiation and (2) magnetic field modulation are conducted. Regarding PMIs, the following elements or processes have been analyzed: (1) boronizations, (2) carbon tile morphology, (3) nitrogen as an impurity, (4) lithium as an advanced PFC, and (5) tungsten as the divertor target.

2 Physics experiments

2.1 ELM simulation in DiPS-2

To simulate both the edge plasmas and ELM phenomena of toroidal devices, we performed experiments exposing the wall and the PFCs, such as carbon and tungsten in DiPS-2, which has edge-relevant physical parameters (steady-state magnetic field up to 1 kG, plasma density (n_e) $\sim 10^{19} \text{ m}^{-3}$, electron temperature (T_e) = 1–15 eV) and geometry (radius of chamber = 102 mm, radius of magnetic nozzle = 25.2 mm, length = 2526 mm), to a transient heat flux. An LaB₆ cathode with a 4 inch diameter disk with 1/4 inch thickness was used in the DiPS-2; it was indirectly heated using a graphite heater. Plasma was produced using a heating power of more than 5 kW (280 A, 18 V) and a discharge power of 3–20 kW (30–100 A, 100–200 V) with argon, helium, and hydrogen gases. The LaB₆ cathode can generate a higher density of thermal electrons than tungsten, and molybdenum, as shown in Fig. 1 and Table 1. The DiPS-2 has a magnetic nozzle to apply a stronger magnetic field in the middle of the device with a limiter structure, which generates a simulated magnetized SOL region in the fusion device. This nozzle has three roles: (1) separating the plasma between the source

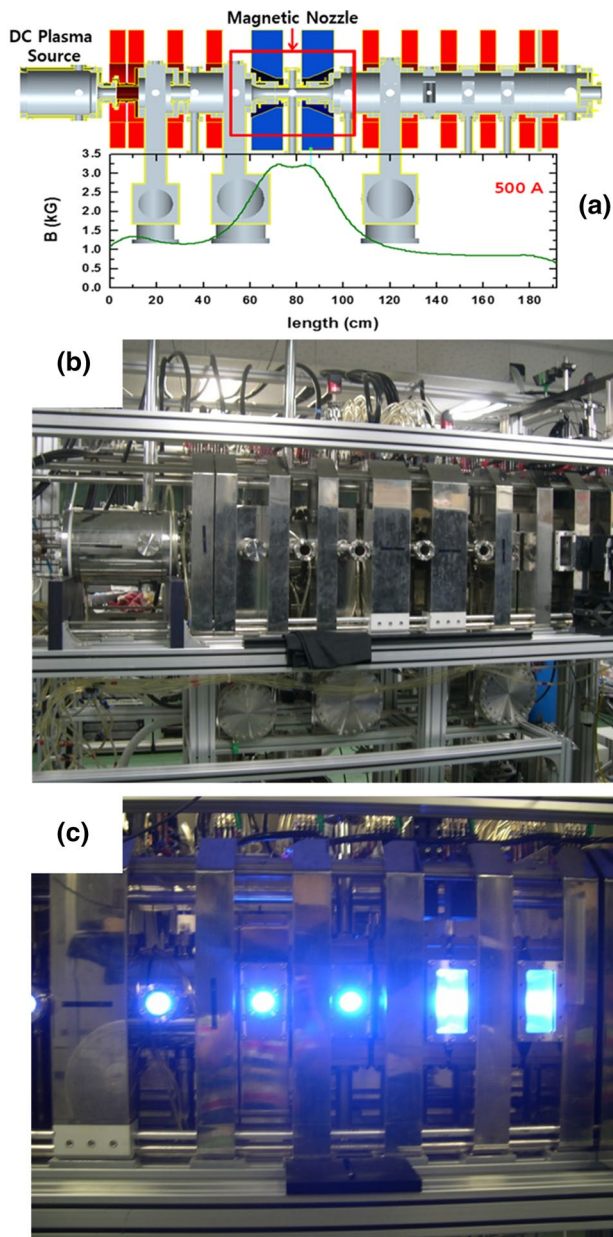


Fig. 1 **a** Schematic view and **b** photograph of the DiPS-2, and **c** operation of the DiPS-2 with an argon plasmas

and the test regions, (2) squeezing the plasma magnetically and geometrically, and (3) forming an SOL-like structure by scraping the source (core) plasma.

Fast-scanning probes (FSPs) and fixed azimuthal probes were installed on the wall of the DiPS-2 to measure the edge and the wall plasma parameters. ELMs were simulated using magnetic modulation in the DiPS-2, as shown in Fig. 2, and transient heat and particle fluxes on the wall were compared with those for the KSTAR device. (1) Magnetic modulation leads to periodic particle and energy release toward the wall, which seems to be similar

Table 1 Specification of plasma parameters in the DiPS-2

Type and name (unit)	DiPS-2 [20, 21]	Tokamak divertor (edge) [22]
ITER ELMs ($\text{MJ m}^{-2} \text{s}^{-1/2}$)	50–100 (laser)	> 50
ITER disruption ($\text{MJ m}^{-2} \text{s}^{-1/2}$)		~ 100
ITER steady state Heat load (MW m^{-2})	~ 0.1–10	> 10
n_e (m^{-3})	10^{17} – 10^{19}	10^{18} – 10^{20}
T_e (eV)	1–20	10–80
T_i (eV)	0.1–0.2	$T_i = T_e$
Γ ($\text{m}^{-2} \text{s}^{-1}$)	10^{22} – 10^{24}	~ 10^{24}
D_{\perp} ($\text{m}^2 \text{s}^{-1}$)	10–80	1–20
B (kG)	1–1.5	10–50

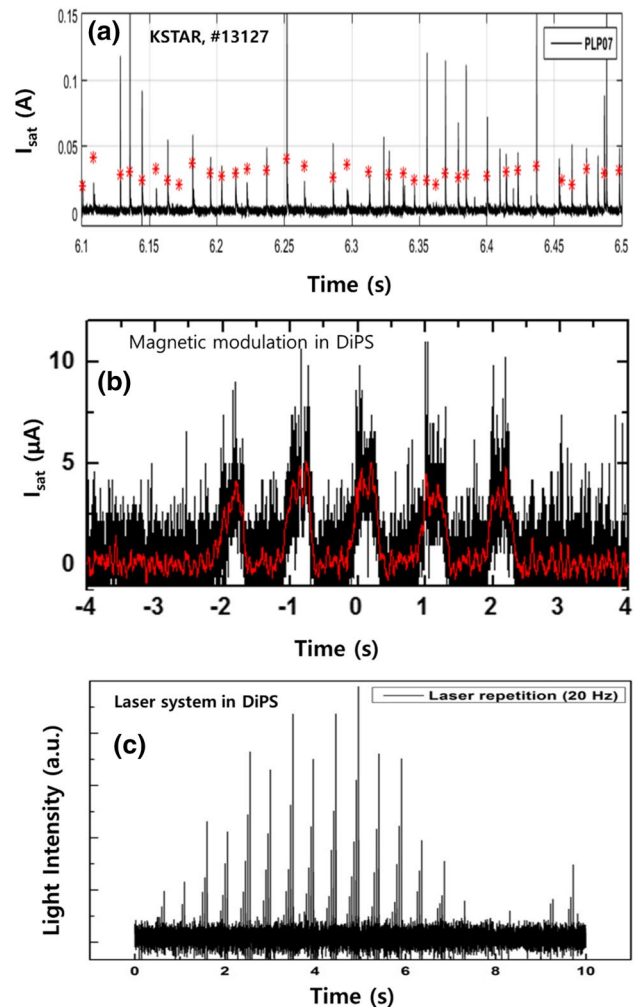


Fig. 2 **a** ELM peaks in KSTAR, **b** ion saturation current peaks obtained using magnetic modulation in the DiPS-2, and **c** reflection light peaks from tungsten target due to laser modulation in the DiPS-2

to the ELM phenomena of toroidal devices in terms of the energy loss rate and the frequency. For magnetic modulation, a programmable power supply was used to control the current applied to the magnets. (2) ELMs were also experimentally simulated using the interaction of a high-energy pulsed laser with tungsten targets in a magnetized plasma in the DiPS-2. (3) The effects of dusty plasma injection on the characteristics of plasma density in magnetized plasmas were estimated under steady state and transient conditions. The transient energy flux of the pulsed laser was $\sim 100 \text{ MJ m}^{-2} \text{ s}^{-1/2}$ per laser shot, and the beam injection frequency was fixed at 20 Hz because type-I ELMs in fusion devices occur at frequencies of approximately 10–200 Hz. The effects of dusty plasma injection on the plasma density of an edge-relevant plasma depended highly on n_e when the ELM-like condition was simulated by exposing a tungsten surface to a pulsed laser beam.

For estimates of the transient or steady-state heat fluxes, an FSP was installed on the side of the DiPS-2 and utilized to obtain radial profiles of plasma density, electron temperature, and heat flux using installed triple probes. Because of the relatively higher plasma density, Debye length (λ_D) was relatively shorter than the probe dimension ($\alpha_p = \text{probe tip area} \approx \text{sheath area}$); therefore, the sheath of the FSP was assumed to be thin ($\lambda_D \ll \alpha_p$). Three thermocouples were also installed at the center of the DiPS-2 to measure the temperature using an infra-red (IR) camera to measure the surface temperature of the tungsten target. Thermocouples (TCs) were inserted at 18 mm, 13 mm and 3 mm beneath the target surface. The target was made of tungsten, with a total thickness of 20 mm to simulate the divertor and the first-wall relevant conditions.

For investigations of the effect of the transient heat flux on the far-SOL and wall regions, experiments were conducted in both the DiPS-2 and the KSTAR. Fast-scanning probes and fixed probes were installed poloidally on the wall of the DiPS-2 to measure the edge and the wall plasma parameters. The transient heat and the particle fluxes on the wall were compared with those for the KSTAR device. In the KSTAR, specific type-I ELMing H-mode discharges were performed with a lower single null magnetic geometry, where the outboard separatrix position was slowly (approximately 7 s) scanned over a radial distance of 7 cm, reducing the wall probe–separatrix distance to a minimum of ~ 9 cm and allowing the ELM filament heat loss to the wall to be analyzed as a function of radial propagation distance. An electric probe was installed at a fixed position toroidally near the wall's poloidal probe and radially located 4.7 cm in front of the wall probe. The measured radial propagation speed and the calculated radial profile of the magnetic connection lengths across the SOL can be utilized to test the filament energy loss model for future machines.

2.2 Transport simulation in DiPS-2

2.2.1 Diffusion (free and bounded presheaths)

For the experimental simulation of the transport phenomena at the edge of fusion toroidal plasmas, a free presheath was generated for comparison with a bounded presheath in a magnetized plasma by inserting a tungsten perturbing object (TPO) into the center of the DiPS-2 main plasma [20]. The plasma parameters at the ram of the TPO and those at the wake showed clear differences from those of normal operating plasmas without a TPO, as shown in Fig. 3. Based on these measurements of the wake of a TPO, the diffusion coefficient (D_{\perp}) and characteristic length of the perturbing or flux tube were investigated using $D_{\perp} = c_s \lambda_{ne} / 2$ and $L_c = a^2 \sqrt{(T_e + T_i) / m_i} / D_B$ where $c_s = \text{Bohm velocity}$, $\lambda_{ne} = \text{decay length of plasma density}$, $L_c = \text{characteristic length of perturbing for flux tube}$, $T_i = \text{ion temperature}$, $m_i = \text{ion mass}$, and $D_B = \text{Bohm diffusion coefficient}$ [20, 23, 24]. The D_{\perp} results satisfied the equation as $D_B = kT_e / 16eB$, showing a dependency on T_e / B . In addition, the normalized factors ($\delta = D_{\perp} / D_B$) were obtained as approximately 8 at a

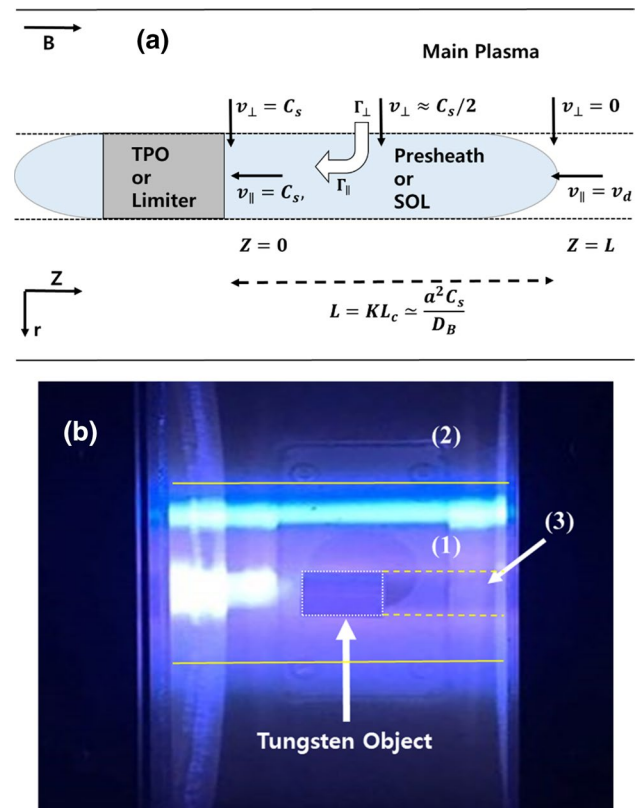


Fig. 3 **a** Concept of free and bounded presheaths using a tungsten perturbing object (TPO) and **b** photograph of experimental results regarding the magnetized plasma in the DiPS-2 with TPO [20]: (1) main plasma stream, (2) bounded presheaths, and (3) free presheaths

free presheath and approximately 11 at a bounded presheath. To consider the transport parameters to calculate L_c at a free presheath, we introduced scale factor (K) as $L = KL_c$, and we obtained $L \sim 10$ cm for a free presheath. Figure 4 shows a comparison of the diffusion coefficients between the DiPS-2 and the fusion devices as a function of the electron temperature/magnetic flux density.

2.2.2 Convection (filament transport)

Heat loads deposited on the first wall using mitigated type-I ELMs are expected to be the dominant contributor to the total thermal plasma wall load of the ITER, particularly in the upper main chamber regions during the baseline H-mode magnetic equilibrium because of the fast radial convective heat propagation of ELM filaments before complete loss to the divertor [25]. From the perpendicular heat flux to the wall and ELM energy loss for a single ELM, we can deduce the values of the magnetic energy density variation using the calculated magnetic modulation (ΔE_B , $B = 1\text{--}2.8$ kG, $\Delta B \sim 65\%$, duration = 0.5 s) as $E_B = B^2/2\mu_0$ and the theoretical

ratio of generated energy $E_{B1}/E_{B0} \sim 12.3\%$, where $B_0 = 2.8$ kG and $B_1 = 1.0$ kG, as shown in Fig. 5. Considering that W_{B1}/W_{B0} is the energy loss to the wall caused by modulation where W_B is energy loss to the wall by magnetic modulation, the experimental results can be compared. The plasma energy at the edge region (E_{edge}), near the wall, is calculated as $E_{\text{edge}} \sim nT_e$, ($T_i \ll T_e$), from the probe measurements. The ratio of the released energy caused by magnetic modulation is $E_{\text{edge},B1}/E_{\text{edge},B0} \sim 1.67\%$. The total plasma energy in the DiPS-2 (W_p) can be written as $W_p = \frac{3}{2}n(T_e + T_i)V_p \sim 80$ mJ, ($T_i \ll T_e$), and the energy loss rate to the wall from total plasma energy resulting from transient heat flux in the DiPS-2 is $W_{\text{wall}}/W_p \sim 0.75\%$, where V_p is plasma potential.

2.3 KSTAR experiments

A set of poloidal electric probes (PEPs) was installed for measurements of the far-SOL parameters of the KSTAR, this set composed of eight electric probes on a rectangular plate with dimensions of 125×280 mm² [25]. The tips of the PEP, are made of a carbon fiber composite and are insulated with boron-nitride covers. The structure of the PEP assembly is illustrated in Fig. 6. The diameter of each probe tip was 4 mm, and it protruded 1 mm from the graphite tile's surface. PEPs were fixed on the outboard mid-plane wall and located 7.5 cm behind the outboard toroidal limiters. These are located ~ 16 cm behind the typical separatrix position of KSTAR diverted plasmas. The tips of the PEP are composed of triple probes (TPs) and one Mach probe (MP), which can directly measure the electron temperature, particle and heat fluxes, and Mach numbers in the far-SOL region at a sampling rate of 2 MHz. Poloidal probes are located slightly upward with respect to the main plasma, as calculated using real-time equilibrium reconstruction code (EFIT). Hence, the upper triple probe can obtain more consistent data. Figure 7 shows the probe tip's position viewed from the plasma and their arrangement, showing that they do not duplicate magnetic field lines. The magnetic field lines were carefully arranged to observe motion like an ELM filament. In the KSTAR, the typical field-line pitch angle ($3^\circ < \theta_{\text{pitch}} < 7^\circ$) can be described as $\theta_{\text{pitch}} = \tan^{-1}(B_\theta/B_\phi)$, which correspond to safety factor (q_s) $\approx rB_\phi/RB_\theta$ as $3 < q_s < 6$. Therefore, there is no self-shadowing for any of the pins of each TP where B_θ = poloidal magnetic field (B_p) and B_ϕ = toroidal magnetic field (B_T). The range of the pitch angle was calculated from 20 shots with various plasma current (I_p) and B_T ($\theta_{r0} > \theta_t > \theta_{\text{pitch}}$).

In the KSTAR, there are two other types of probes located at different locations from the PEP. Approximately 100 fixed electric probes (FEPs) are installed poloidally on the inboard limiter and divertor tiles at the C bay of the KSTAR vacuum vessel to measure the basic plasma parameters and

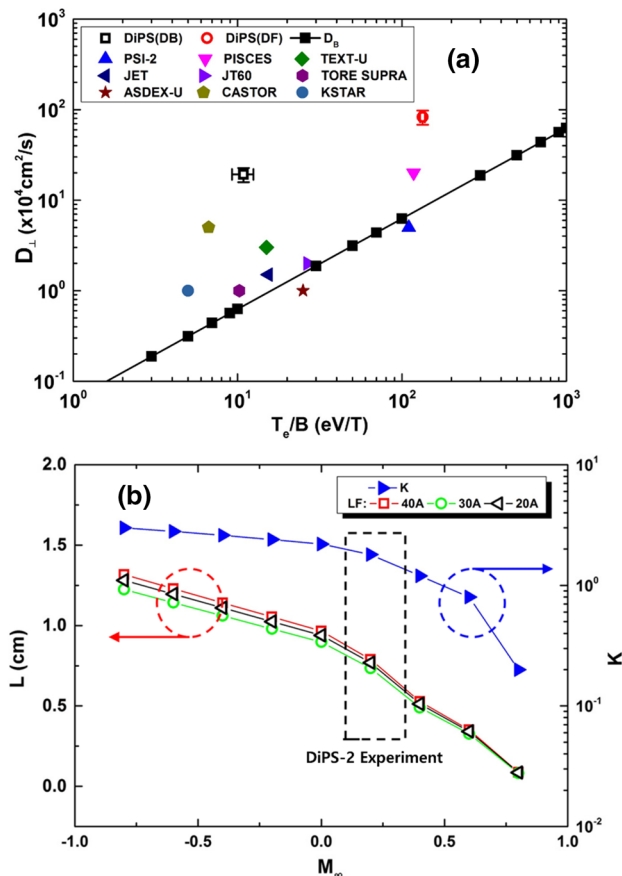


Fig. 4 a Comparison of diffusion coefficients between the DiPS-2 and fusion devices as a function of electron temperature/magnetic flux density [20]

Fig. 5 Experiment on filament transport with poloidal electric probes in **a** the DiPS-2 and **b** KSTAR

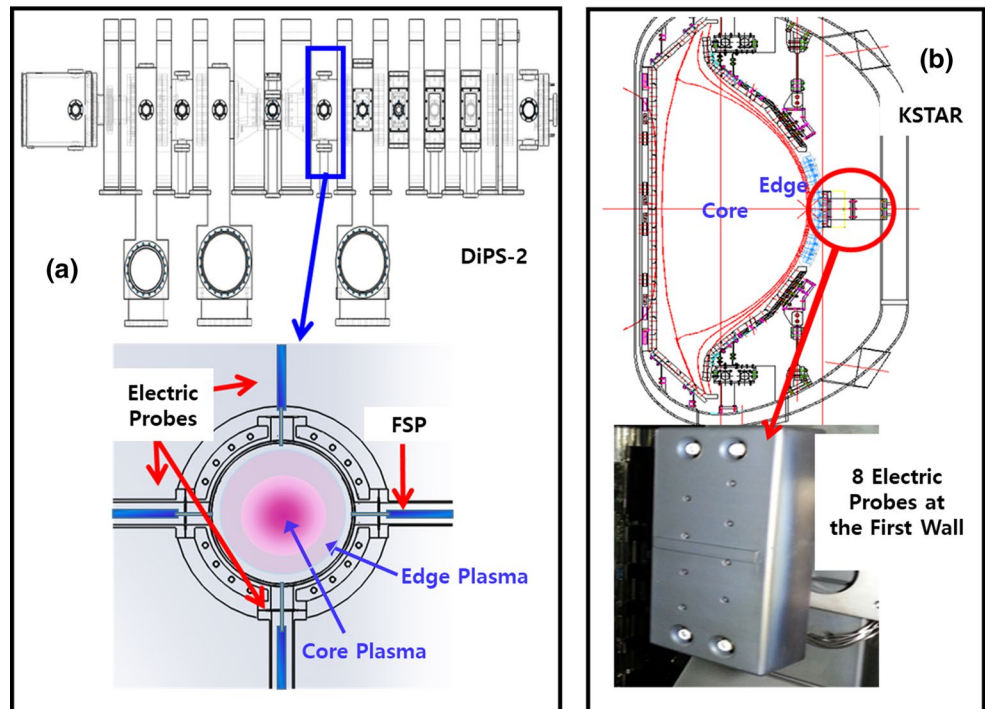
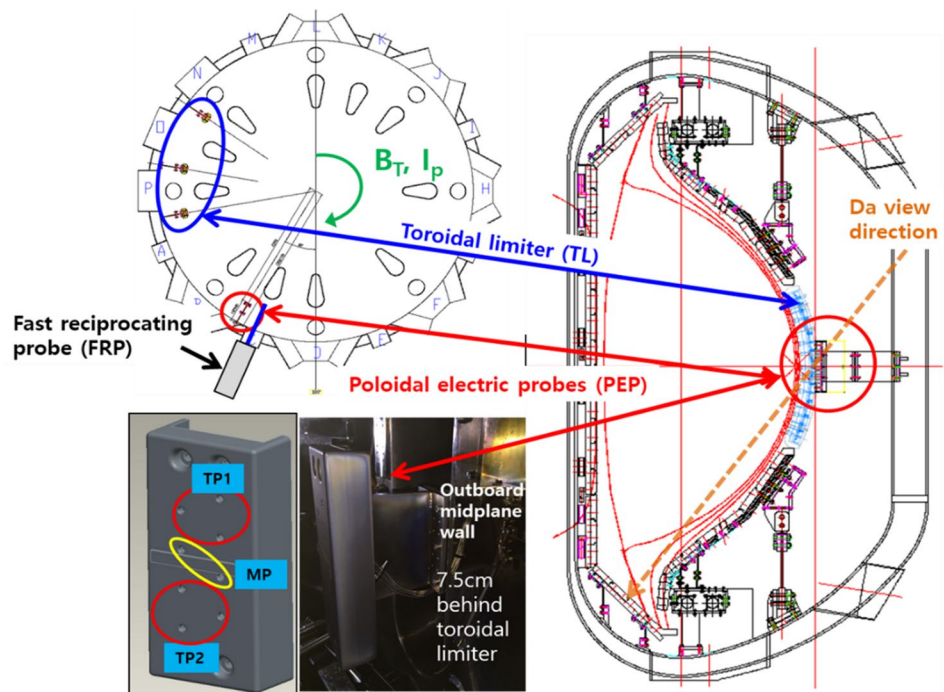


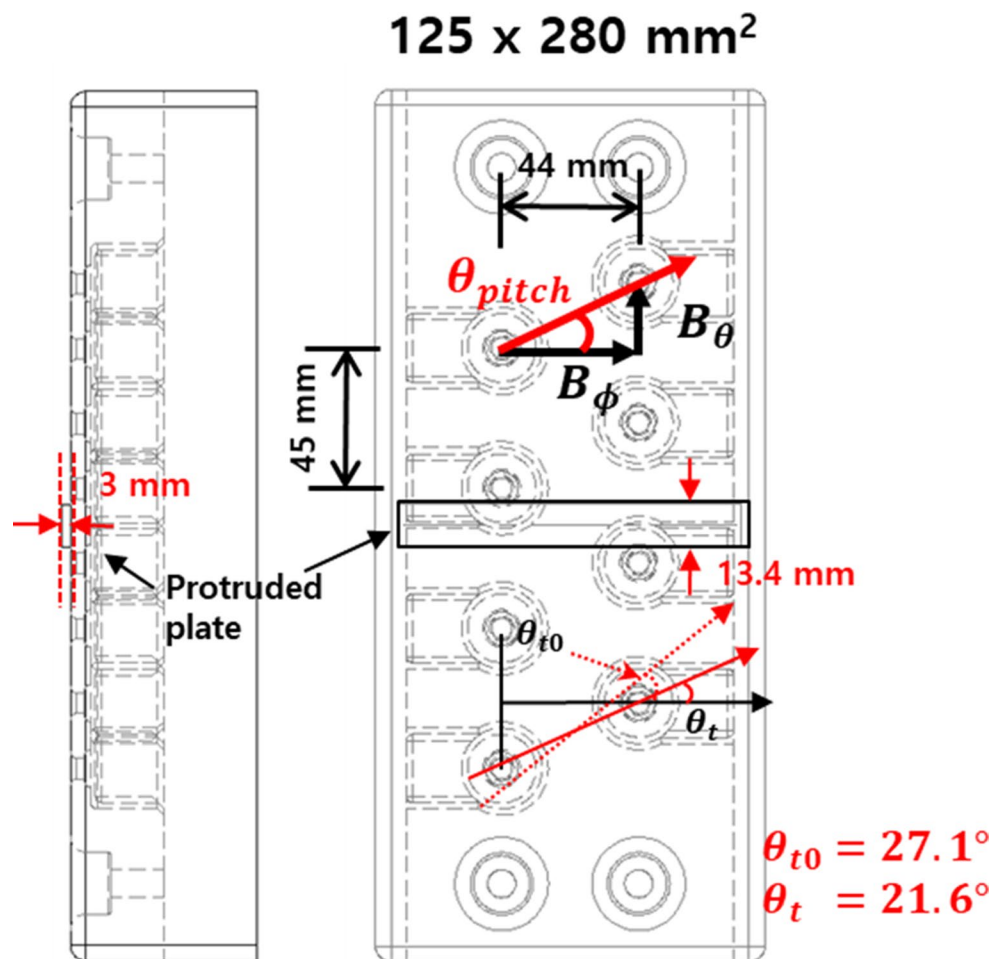
Fig. 6 Horizontal and vertical cross sections of KSTAR and positions of FRP, toroidal limiter, and PEP. The dark green dashed line indicates the D_a view direction (DVD), (B_T =toroidal magnetic field, I_p =plasma current) [25]



their poloidal profiles in the inboard limiter and divertor regions. A fast-reciprocating probe (FRP) is installed on the C-port mid-plane to measure the spatial profile of the edge plasma. The length of the FRP shaft is approximately 200 cm, and the stroke distance from the wall to the plasma edge is approximately 100 cm. The maximum speed of the

FRP is up to 1.8 m s^{-1} . Both probe tips are made of carbon fiber composite and insulated with boron-nitride covers. The angle between the poloidal magnetic field and the probe's tip changes according to the plasma control conditions, and the incident angle of the particles also changes. Because the effective area of the probe tip varies with the changing

Fig. 7 Technical drawing of the poloidal electric probe. The tip positions have been arranged considering self-shadowing



angle, it is fabricated in a dome shape to minimize the error in consideration of the incident angle of the particle.

As shown in Fig. 8, the data from the FEP and the FRP showed that decay length of electron temperature (λ_{Te}) and decay length of plasma density (λ_{ne}) are 2–4 cm and 1–3 cm, respectively [26]. The magnitude of parallel flow velocity ($v_{||}$) near the last closed flux surface (LCFS) was 4–15 km s⁻¹. The radial flux caused by edge turbulence in the SOL region was investigated using a spectral analysis of electrostatic fluctuation levels, such as ion saturation current (I_{sat}) and floating potential (V_f) obtained from the fast-reciprocating Langmuir probe assemblies (FRLPA) measurement. The value of the flux was estimated to be approximately 10²⁰ m⁻² s⁻¹ near the LCFS. With improved FEP and FRP, during L-mode with inner wall limited plasma ($B_T=2.0$ T, $I_p=0.4$ MA), λ_{Te} and λ_{ne} , which are the e-folding lengths in the main SOL region, are evaluated as 3.5 cm and 2.1 cm, respectively [27]. From particle flux measurements at the far SOL region during a diverted ELMy H-mode discharge ($B_T=1.8$ T, $I_p=0.65$ MA), the peak heat flux toward the outboard wall during ELM bursts is estimated to be up to ~20 kW m⁻², which may be less than 1% of the

peak divertor heat flux expected for the NB heating power of ~2.66 MW and a stored energy (W_{TOT}) of ~0.38 MJ.

3 Plasma–material interactions

3.1 Boron

Carborane (C₂B₁₀H₁₂), a non-toxic boron-containing material, has been used to deposit amorphous hydrogenated carbon/boron (a-C/B:H) thin films using helium DC glow discharges in Dust interaction with Surface chamber (DiSC) [28]. A helium plasma was produced in the pulsed mode at a duty cycle of 0.375 (3 s on/5 s off) or 0.23 (3 s on/10 s off) using a filament discharge connected with a carborane evaporation source at a target pressure of ~5 mTorr. Deposited a-C/B:H thin films were analyzed using variable angle spectroscopic ellipsometry, Auger electron spectroscopy, scanning electron microscopy, and X-ray photoelectron spectroscopy. The a-C/B:H thin films show soft polymer-like characteristics with optical constants of $n_t=1.65$ and $k_t=10^{-3}$ at 632 nm, and the B/C

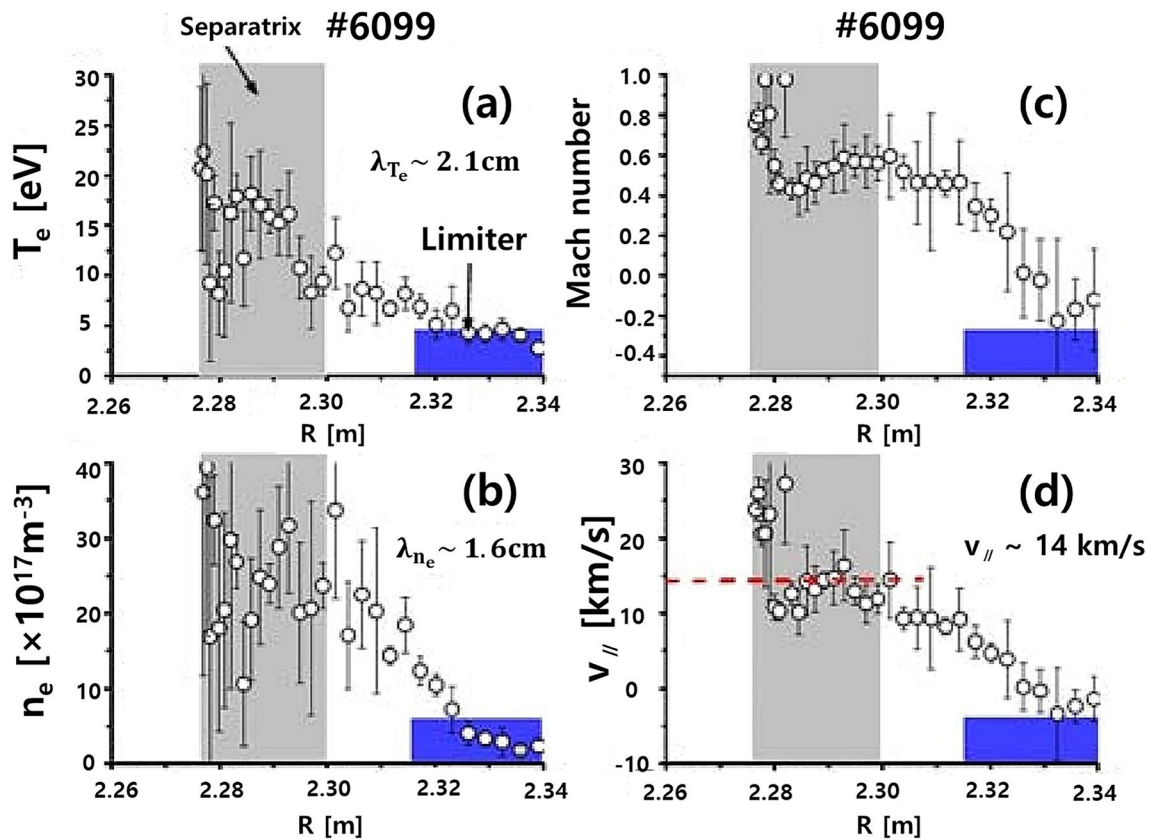


Fig. 8 Radial profiles from the FRLPA measurement in the SOL region during an H-mode discharge: **a** electron temperature, **b** plasma density, **c** Mach number, and **d** parallel flow velocity [26]

ratio inside the bulk is approximately 2 for an approximately 60% boron content.

The evaporation characteristics of the carborane powder under vacuum were analyzed. Deposited boron-containing films show polymer-like thin film characteristics with a cauliflower-shaped surface structure, and the surface roughness increases with the thickness. Because the deposition mechanism is dominated by low-energy ions, radicals, and neutrals, the films are not affected by the position inside the vacuum chamber or the duty cycle. The first boronization was performed in the KSTAR tokamak during the 2009 campaign to reduce oxygen impurities and to decrease the power loss caused by radiation [29]. The results from the experiments with carborane during the first boronization in KSTAR have been reported. After boronization, the levels of water and oxygen in the vacuum vessel were reduced drastically. The deposited thin films were characterized using variable-angle spectroscopic ellipsometry, X-ray photoelectron spectroscopy (XPS), and Auger electron spectroscopy (AES). The carbon flux on the wall was deduced to be approximately $1.78 \times 10^{16} \text{ cm}^{-2} \text{ s}^{-1}$ using a cavity technique.

3.2 Carbon

A carbon/graphite tile as a PFC was irradiated with a helium plasma of high flux and low energy in the DiPS-2, and the damage to the graphite-tile target was investigated [30]. Changes in surface morphology were observed using scanning electron microscopy (SEM). As Fig. 9 shows the electrical conductivity was decreased according to the four-probe measurements, and the intensity of the graphite disorder peak was increased, as shown using Raman spectroscopy. In addition, the electrical conductivity decreased from 520 to $220 \text{ } \Omega^{-1} \text{ cm}^{-1}$ because of a combination of morphology degradation and induced structural disorder.

3.3 Nitrogen

Nitrogen gas was injected at a rate of 2.5–30% as an impurity into the helium plasma in the DiPS-2 with a LaB_6 cathode to determine the effects of nitrogen on the heat flux to the PFCs and on the plasma parameters. Pure helium plasma had the following parameters: $T_e \approx 12.5 \text{ eV}$ and $n_e \approx 1.4 \times 10^{17} \text{ m}^{-3}$. To evaluate the plasma heat flux toward tungsten, as shown in Fig. 10a, the following diagnostics: (1) TCs were located

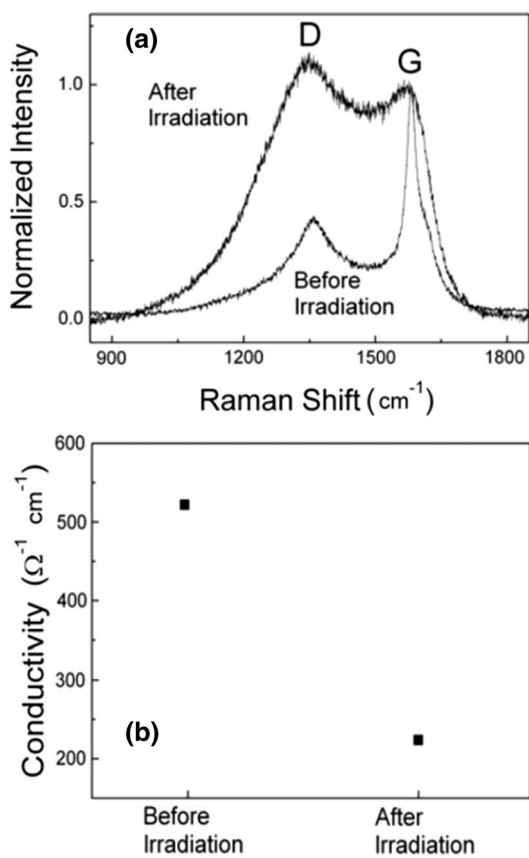


Fig. 9 a Raman spectra, and b electrical conductivities of the graphite-tile target before and after helium-plasma irradiation [30]

inside the tungsten target to estimate the inner temperature of the tungsten, (2) an IR camera was used to detect the surface temperature of tungsten, (3) and a TP was used to determine the electron temperature and density, which were also compared with those measured using a single electric probe. The heat flux (q_c) was calculated from a steady-state conduction equation, which is approximately given as:

$$q_c = -k_h \frac{\partial T}{\partial x} + \rho c_h \frac{\partial T}{\partial t} \approx -k_h \frac{T_B - T_A}{x_B - x_A}, \tag{1}$$

where $T_{A,B}$: the temperature at the position of $A(=x_A)$ or $B(=x_B)$, k_h : thermal conductivity, ρ : mass density, and c_h : specific heat of the material. To calibrate the temperature of IR camera, was applied the emissivity of tungsten to IR camera measurement system, and its temperature was calibrated using the initial temperature of the TC. Previous works, such as the configuration of a diagnostics system, experimental setup, and comparison results for effect of nitrogen on the heat flux to a tungsten target in a helium plasma using three methods were reported in detail [31]. The results for comparison of the heat fluxes measured by the three methods with variation of impurity rate are shown in Fig. 10b. With

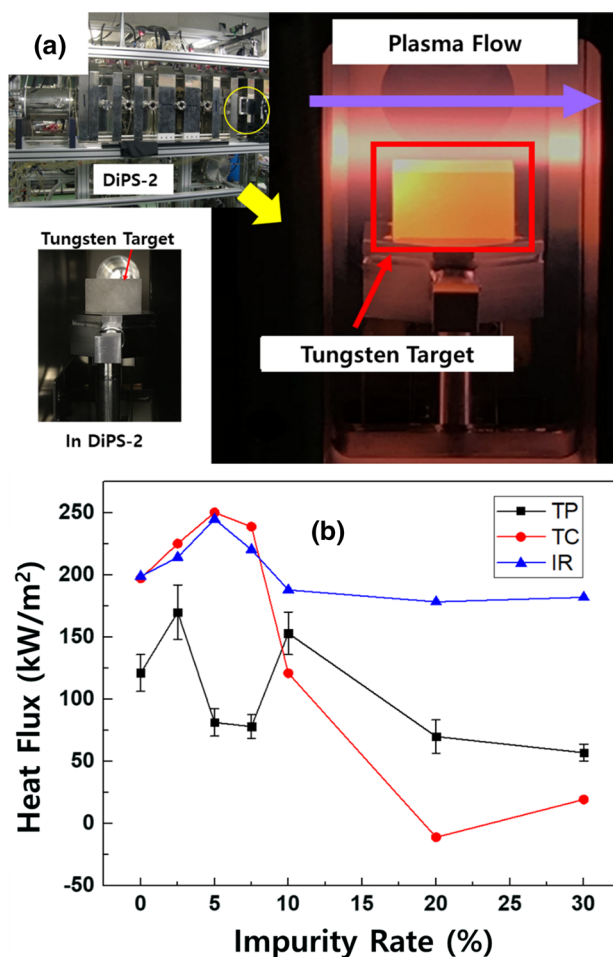


Fig. 10 a Experimental setup to determine the effect of nitrogen on the heat flux to a tungsten target in a helium plasma and b comparison of heat fluxes obtained using three measurement methods (TP, TC, and IR camera) at the impurity rate is changed from 0 to 30%: TP's are those using a triple probe, TC's are those using a thermocouple, and IR's are those using an IR camera [31]

nitrogen injection, the plasma parameters decreased: density by 60% and the electron temperature by 20%, leading to a gradual decrease in the heat flux. Heat fluxes measured using the three different methods (TC, IR camera, and TP) were compared with one another. The IR camera and TC data showed a similar tendency while the uncertainty between them increased with increasing impurity rate. The maximum uncertainty in heat fluxes between the IR camera and TP methods at an impurity flow rate of 30% as an approximately 160%.

3.4 Lithium

For the development of efficient lithium injection, the density profiles of lithium vapor of the Lithium Injection Gettering of Hydrogen and its Transport experiments-1

(LIGHT-1) device were analyzed, and a lithium injector for the large helical device (LHD) was tested: (1) radial and axial variations in the densities of lithium neutrals and ions were analytically calculated for a cylindrical chamber by assuming classical diffusion with or without a magnetic field

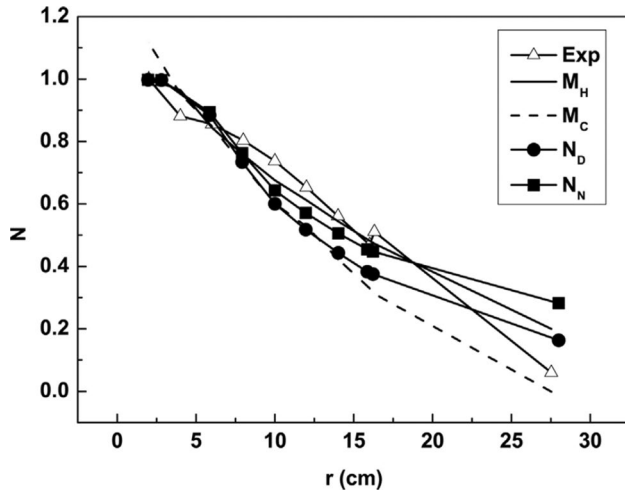
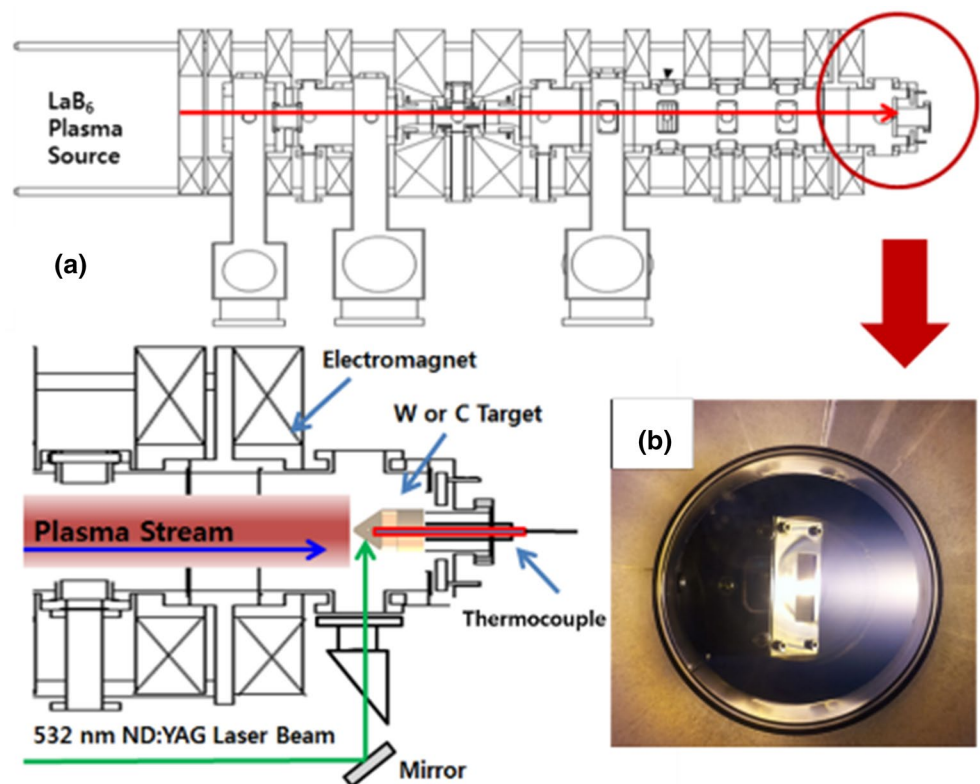


Fig. 11 Fitting of experimental data to analytic solutions for the fluid model and the Monte Carlo code (hot and cold nozzles) with the following conditions: relaxation length $R=25$ cm, r_1 (radius of neutral lithium source at $z=50$ cm (at the location of the movable deposition probe)) = 5.0 cm, and r_2 (radius of LIGHT-1 device) = 50 cm [32]

Fig. 12 **a** Schematic view of an experimental set-up in the DiPS-2, and **b** photograph of helium plasma irradiation in the DiPS-2



(B) [32]. Neutrals and ions without B can be expressed as a linear combination of the modified Bessel functions of order zero (I_0 and K_0) while ions with B can be expressed as their square root. Analytical solutions for the lithium neutral densities with Dirichlet and Neumann boundary conditions were compared with those obtained using Monte Carlo simulations and experimental values for the LIGHT-1 device. Proper combinations of the relaxation length and the size of the source produce well-fitted profiles similar to those observed experimentally and those obtained using Monte Carlo codes, as shown in Fig. 11. (2) The method of lithium dispersion was investigated under the assumption that the experiment was carried out in the LHD at the National Institute for Fusion Science, Japan [33]. A performance test was performed on a prototype of a vapor injector. The amount of injected lithium was approximately 1% of the value expected from the vapor pressure data because of the generation of lithium oxide. The nozzle temperature was also found to be quite important for suppressing Li dispersion.

3.5 Tungsten

3.5.1 Tungsten damage

Figure 12 shows the experimental setup of a simulated ELM with a pulsed laser in the DiPS-2. The tungsten target has the following specifications: size = 25×25 mm², made in

Russia, density 19.20 g cm^{-3} , hardness: 453 HV30, and tungsten: 99.95%. The helium plasma density and electron temperature were measured using the triple probe on the fast-scanning system. The plasma has the following specifications: $n_e = 3\text{--}6 \times 10^{18} \text{ m}^{-3}$ and $T_e = 5\text{--}10 \text{ eV}$ at a base pressure of $8 \times 10^{-7} \text{ Torr}$, a working pressure of $7 \times 10^{-4} \text{ Torr}$, and a magnetic intensity of 0.7 kG. The heat load is approximately $1\text{--}10 \text{ MW m}^{-2}$, similar to the steady-state plasmas of the ITER divertor. An Nd:YAG pulsed laser is used as the source of transient heat loads, like ELMs on tungsten targets in plasmas, with the following specifications: wavelength = 532 nm, pulse width = $\sim 10 \text{ ns}$, maximum energy = 250 mJ, and beam diameter = 5 mm. The variation in the heat flux factors (F_{HF}) is proportional to a given transient heat pulse for the possible worst case of energy densities during transient events in the ITER; $F_{\text{HF}} = q_{\perp} T_{\text{trans}}^{-1/2}$, where q_{\perp} is the perpendicular energy density on the target surface, and $T_{\text{trans}}^{-1/2}$ is the heat pulse duration of transient heat loads to the targets, depending on the incidence angle [21]. For the laser alignment with targets irradiated by plasmas, the incidence angle of a pulsed laser to the targets is fixed at 45° , which is $\sim 100 \text{ MJ m}^{-2} \text{ s}^{-1/2}$ per laser shot considering the heat flux factor. The tungsten targets, kept at 300°C , by water cooling, as measured using K-type thermocouples, were irradiated with a helium plasma for approximately 5 h for long-term operation of a fusion device, with 200–500 shots of a pulsed laser that has 20 Hz pulse frequency. The change in the surface layers and structures were investigated using SEM.

SEM micrographs of the experimental results are shown in Fig. 13. The tungsten targets damaged using a pulsed laser were clearly different from the non-irradiated targets because the structural changes were caused by melted

layers of the original surface or losses to dust clusters. After irradiation of the tungsten targets in a plasma using a pulsed laser, the micro-sized melt layers appeared as if they were moving one direction, along the plasma stream, against the vertical gravitational force, as shown in Fig. 13b and c. In the case of targets irradiated using a pulsed laser, micro-sized cracks and the recrystallization of tungsten targets, which appear to have a striped pattern with a nanoscale, were observed, as shown in Fig. 13e and f.

For a comparison of the transient effects on the tungsten targets in a high-density plasma (particle flux: $\sim 10^{23} \text{ m}^{-2} \text{ s}^{-1}$) with low-density plasma (particle flux: $\sim 10^{18} \text{ m}^{-2} \text{ s}^{-1}$), an experiment with a DC filament discharge source ($n_e: \sim 10^{15} \text{ m}^{-3}$, $T_e: 1\text{--}3 \text{ eV}$ at a working pressure of $3 \times 10^{-4} \text{ Torr}$), which was used after the interaction of laser irradiation with targets to monitor plasma fluctuations using electric probes, was conducted, and results are as shown in Fig. 14. Figure 15 shows the effects of laser irradiation on tungsten targets in a low-density plasma with high-density plasma. Both cases clearly show significant changes in the surface structure. The striped pattern and the melt layer motions along the plasma stream were not apparent in the case of a low-density plasma. The melt layer motion and stripe patterns on the tungsten surface were caused by the effects of the pulse laser and high-density plasma irradiations at the same time because there were no effects on only plasma irradiation, as shown in Fig. 15d, and the pulse laser with a low-density plasma irradiated the tungsten target at the same time, as shown in Fig. 15a and c. These results show that the parameters of the background plasma are important for the deformation of tungsten targets when transient heat fluxes, such as those in ELMs, occur.

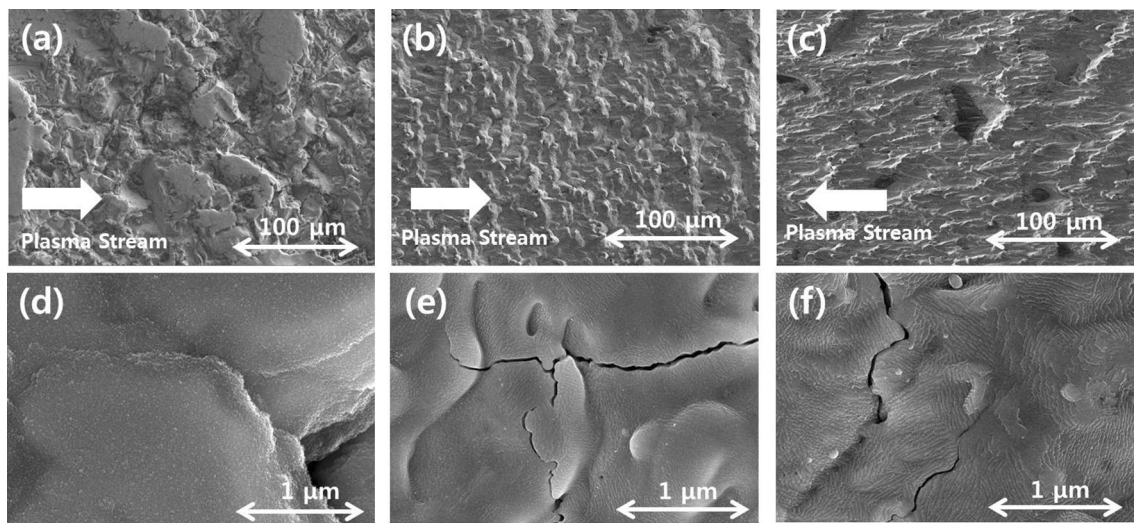


Fig. 13 Tungsten targets exposed to plasmas with laser irradiation. SEM images on a 100- μm scale: **a** 0 shots, **b** 200 shots, and **c** 500 shots. SEM images on a 1- μm scale: **d** 0 shots, **e** 200 shots, and **f** 500 shots

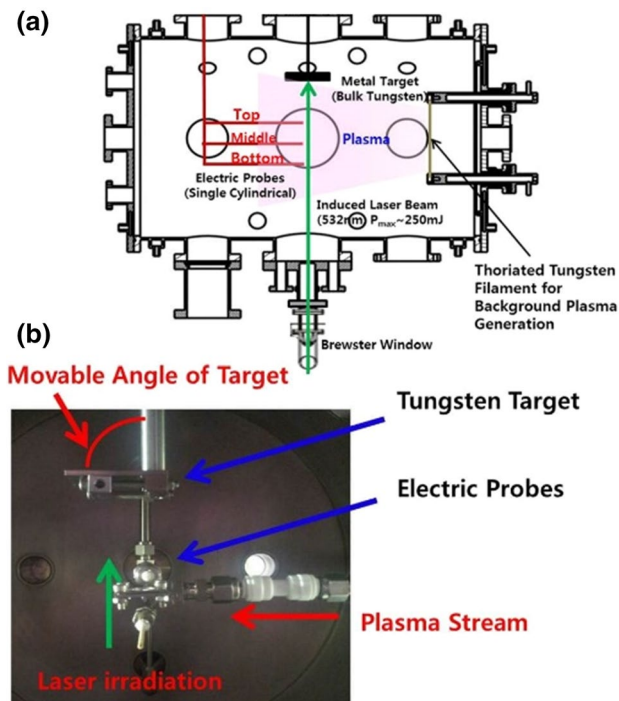


Fig. 14 **a** Experimental set-up for a low density plasma generated using a DC filament source for the monitoring laser-induced plasma and comparing the effects of low- and high-density plasmas and **b** photograph of the experimental set-up in a vacuum chamber

3.5.2 Tungsten dust

The generation of tungsten dust was experimentally investigated by exposing tungsten targets from a F_{HF} simulated using a high-energy pulsed laser so that the rate of dust generation could be analyzed as dust generation is still possible during severe transient phenomena in fusion devices, although plasma-facing components composed of tungsten are less likely to generate dust when compared with other materials. The rate of dust generation is observed to increase linearly with respect to F_{HF} :

$$G[\text{mg}/\text{min}] = C(F_{EX} - F_0), \quad (2)$$

where F_{EX} is the experimental value of F_{HF} , F_0 is the threshold (F_{HF}), and $C[\text{mg m}^2 \text{s}^{1/2} \text{min}^{-1} \text{MJ}^{-1}] = 0.0031 \pm 0.0002$. F_{HF} indicates that the characteristics of dust, such as size, and the value of F_{HF} are similar to those observed in several toroidal fusion devices. The threshold of F_{HF} for dust generation was also observed to be $41 \text{ MJ m}^{-2} \text{s}^{-1/2}$, which is similar to that in the ITER ($50 \text{ MJ m}^{-2} \text{s}^{-1/2}$). If the environments with ELM-like conditions with a transient heat flux of $\sim 100 \text{ MJ m}^{-2} \text{s}^{-1/2}$ in the same volume of the ITER chamber are assumed to be similar, an approximate estimate of dust generation, considering the area ratio between beam irradiation and the ITER chamber, was compared with the data given by the ITER team [34], as shown in Fig. 16.

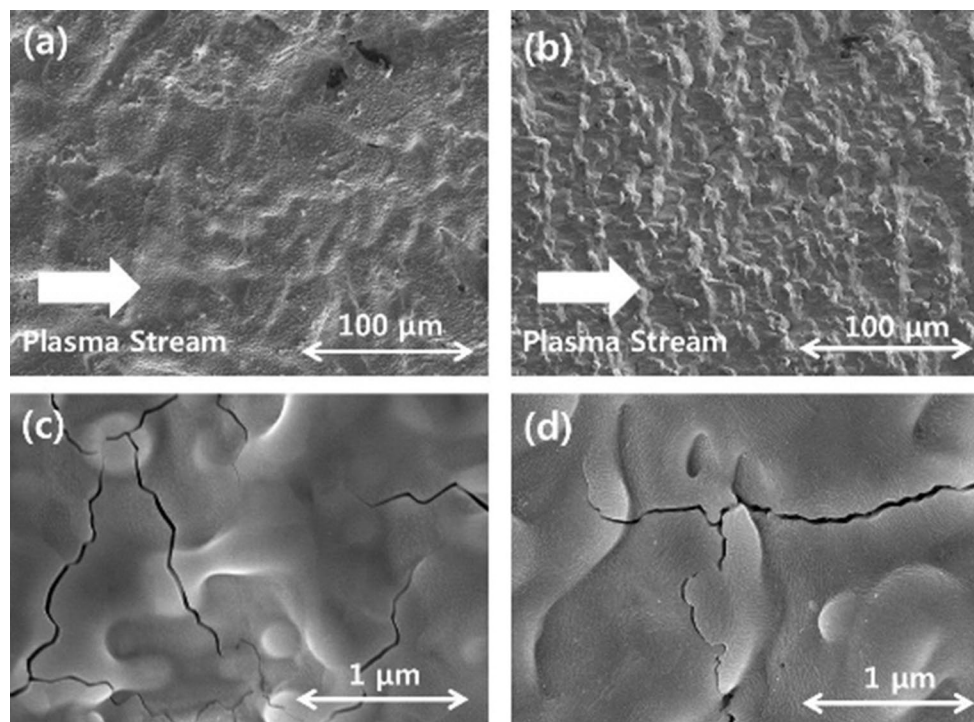


Fig. 15 Surface morphologies of the tungsten target. SEM images on a $100 \mu\text{m}$ scale: **a** in a low-density plasma and **b** a high-density plasma. SEM images on a $1\text{-}\mu\text{m}$ scale: **c** in a low-density plasma and

d a high-density plasma. Both cases are after laser irradiation of 200 shots at an incidence angle of 45°

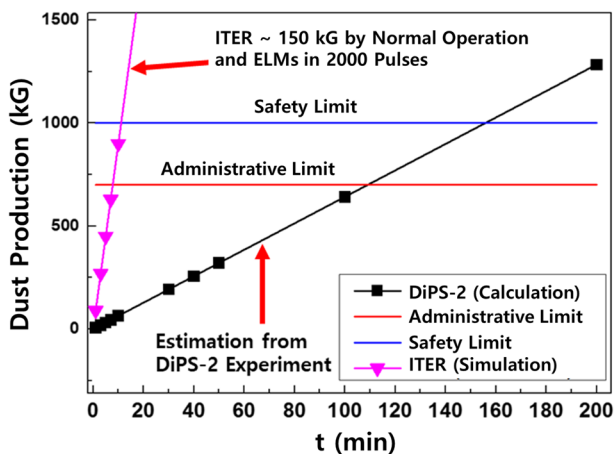


Fig. 16 Comparison of dust production between experiments in the DiPS-2 and the ITER

4 Simulation of transient heat flux (ELMs)

Type-1 and -3 ELMs prevail among approximately five ELMs, the first of which has a large amplitude but lower frequency (f_{ELM} , ELM frequency = 1–100 Hz), with a crash occurring on a short timescale (100–300 μ s) and a power of 10–15% the pedestal power; the other has low amplitude and higher frequency ($f_{ELM} = 10^2$ – 10^3 Hz) with less energy dumped to the divertor ($W_{ELM} = 1$ –5% W_{ped}) [35]. For a linear machine to simulate the ELMs of the ITER or relevant machines, it must be capable of producing similar power to the tungsten target with plasma conditions similar to those of tokamaks: $T_i \sim T_e = 1$ –100 eV and $n_e = 10^{-18}$ – 10^{-20} m^{-3} for the background plasma without ELMs. Most linear machines can produce similar densities, but not similar temperatures ($T_e = 1$ –10 eV, $T_i = 0.01$ – $0.1T_e$) [36–38]. Although we could compromise for the electron temperature by operating the machines much longer than the tokamak operation to provide similar power or heat deposition to the divertor, it is not easy to increase the ion temperature, although there have been exceptions in PSI-2 and Gamma-10 devices: $T_i \sim 2/3T_e$ (PSI-2) [15], T_i for parallel (E-divertor) = 100–400 eV ($T_e \sim 100$ eV, T_{i0} (central cell) ~ 5 keV, Gamma-10) [39]. A report on NAGDIS-2 with a high ion temperature has also been published: $T_i \sim T_e$ (via He II broadening [14]). Regarding the type-I ELM/VDE damage simulation where VDE is vertical displacement events, the Juelich group performed material damage experiments using a high-power laser, electron beam, or arc (torch) plasma [40–43]. Although the net energy/power input to the target could be simulated with respect to the laser and the electron beams, the synergetic or accumulated effect of a plasma with a wide spread of energetic charged particles

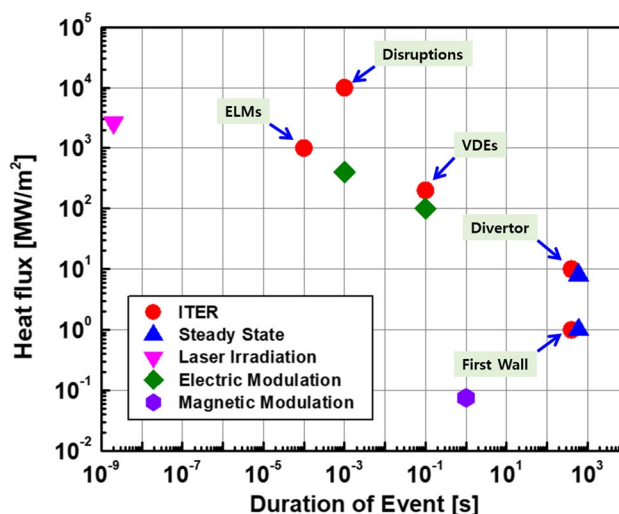


Fig. 17 Comparison of heat flux between the DiPS-2 and the ITER [44, 45] according to the duration of the event. For experimental simulations of the transient and the steady-state heat fluxes, the DiPS-2 was used for experimental simulation with the following specifications: laser irradiation ($q \sim 2.5$ $GW m^{-2}$, $\Delta t \sim 2 \times 10^{-9}$ s, $F_{HF} \sim 1$ –100 $MJ m^{-2} s^{-1/2}$), magnetic modulation for filament experiment ($q = 0.75\%$ of steady state condition, 7.5×10^{-2} $MW m^{-2}$, $\Delta t \sim 1$ s), pulsed high electric modulation ($q = 0.1$ – 0.6 $GW m^{-2}$, $\Delta t \sim 10^{-3}$ s), and steady state condition ($q > 1$ –8 $MW m^{-2}$, $\Delta t > 400$ s)

($0 < \text{kinetic energy} < 100$ keV) would differ from those of a mono-energetic beam.

Figure 17 shows a comparison of the heat flux between the DiPS-2 and the ITER according to the duration of the event. The specifications of the devices are as follows for ITER [44, 45]: ELMs ($q \sim 1$ –10 $GW m^{-2}$, $\Delta t \sim (0.1$ – $0.5) \times 10^{-3}$ s, $F_{HF} \sim 1$ –100 $MJ m^{-2} s^{-1/2}$), VDEs ($q = 0.2$ – 0.6 $GW m^{-2}$, $\Delta t \sim 0.1$ – 0.3 s), disruptions ($q > 10$ $GW m^{-2}$, $\Delta t \sim 0.1$ – 5×10^{-3} s), first wall in a steady-state condition ($q > 1$ $MW m^{-2}$, $\Delta t \sim 400$ s), and divertor in a steady-state condition ($q > 5$ –20 $MW m^{-2}$, $\Delta t \sim 400$ s). For experimental simulations of the transient and the steady-state heat fluxes, the DiPS-2 was used with the following specifications: laser irradiation ($q \sim 2.5$ $GW m^{-2}$, $\Delta t \sim 2 \times 10^{-9}$ s, $F_{HF} \sim 1$ –100 $MJ m^{-2} s^{-1/2}$), magnetic modulation for filament experiment ($q = 0.75\%$ of steady state condition, 7.5×10^{-2} $MW m^{-2}$, $\Delta t \sim 1$ s), pulsed high electric modulation ($q = 0.1$ – 0.6 $GW m^{-2}$, $\Delta t \sim 10^{-3}$ s), and steady state condition ($q > 1$ –8 $MW m^{-2}$, $\Delta t > 400$ s).

4.1 ELM simulation by laser irradiation

When a similar environment with the interaction of ELMs on first walls in the ITER was experimentally simulated using the interaction of a high-energy pulsed laser with tungsten targets in a magnetized plasma in the DiPS-2, the effects of dusty plasma injection on the characteristics of

the plasma density were estimated under steady-state and transient conditions [21]. The full tungsten targets, which had the same specifications as those at the KSTAR, were located at the 4° – 5° magnetic field line so that they would have the same experimental conditions as a tungsten monoblock at the $\sim 3^\circ$ – 4° magnetic field line angle of incidence in the baseline ITER plasma. Because the generated dusty plasma strongly depends on the absorbed laser energy, and the melting threshold of the tungsten walls for the ITER is given as the heat flux factor for the transient damage threshold ($F_{\text{HF}} = q_{\perp} T_{\text{trans}}^{-1/2}$) $> 50 \text{ MJ m}^{-2} \text{ s}^{-1/2}$ per transient heat flux, such as that for ELMs [22, 25, 41, 46], the transient energy flux of the pulsed laser was set at $\sim 100 \text{ MJ m}^{-2} \text{ s}^{-1/2}$ per laser shot. In addition, the beam injection frequency was fixed at 20 Hz because these quasi-periodic bursts in fusion devices occur at a frequencies of approximately 10–200 Hz, denoted “type-I ELMs”. The incident angle of the dusty plasma injection to the background plasma was fixed at 90° . The input rates and the sizes of dust particles were assumed from the measured results ($3 \mu\text{g s}^{-1}$ and 1 – $10 \mu\text{m}$) [21]. For an estimate of the effects of dusty plasma injection (refer to Fig. 18) on edge plasmas, when ELMs $\sim 100 \text{ MJ m}^{-2} \text{ s}^{-1/2}$ with 20 Hz interact with the first walls or a divertor in tokamaks, one wave of plasma parameters of $\sim 0.1 \text{ ms}$ was produced, which consistently results in a perturbation of $\varepsilon_n(\%) = |(n_0 - n_E)/n_0| \times 100 \approx 10\%$ in the core region of steady-state plasmas with $n_e = 1$ – $5 \times 10^{11} \text{ cm}^{-3}$, where n_0 and n_E are the plasma densities of pure plasmas and plasmas with ELM-like conditions, respectively [21].

4.2 ELM simulation using magnetic field modulation

An ELM (particle energy/heat ($p = nT$) fluctuation at the boundary of the SOL) is simulated by modulating the magnetic field (magnetic energy fluctuation), which is considered to be equivalent to a variation in particle energy ($\Delta P \sim \Delta B^2/2\mu_0$) to generate the transient heat flux to the first wall of DiPS-2. It has a magnetic nozzle

for the formation of a magnetic hill and geometrical production of a bounded presheath, which experimentally induces an environment more similar to that of the magnetized plasma in SOL region in a fusion device. In addition, this magnetic nozzle with $B_n = 3.5 \text{ kG}$ can simulate ELM phenomena by changing its ratio to that (B_0) of the test region, i.e., $1 \leq B_n/B_0 \leq 30$. The mild toroidicity can be compensated by controlling discharge current (I_{dis}) to change B_p with z-axial magnetic field (B_z). For example, consider a normal operation condition for the DiPS-2 with $T_e \sim 1$ – 20 eV , $n_e \sim 10^{12} \text{ cm}^{-3}$, $B_z \sim 0.1$ – 1 kG , $r \sim 1 \text{ cm}$, $I_p \sim 1$ – 100 A , and $B_p (= \mu_0 I_p / 2\pi r)$, where μ_0 is the permeability of free space) ~ 0.1 – 10 G . $B_p/B_z \sim 0.01$ – 0.1 can be achieved, which leads to $q_s = 3$ – 30 with an aspect ratio ≈ 3 , indicating typical validity of an experimental approach to investigate phenomena in a fusion plasma using the DiPS-2. For the investigation on heat fluxes on the wall of the DiPS-2 and simulate ELM phenomena, the magnetic field in the nozzle region was modulated by changing B_n with a frequency of $f(\Delta B) \approx 2 \text{ Hz}$ and with variation of $\Delta B/B_0 \approx 0.65$. The maximum adjustable range of the magnetic field that can be maintained in the plasma is 1 – 2.8 kG . Figure 19 indicates the modulated magnetic field at the center by changing the magnetic coil current (50 – 200 A) in the nozzle region. The maximum modulation pulse width is 0.5 s because of the limitation of the response time of the power supply for B_n .

Figure 20a and b show triple probe measurements during magnetic modulation in the DiPS-2. Although differences in the physical properties of ELM occur at steep edge gradients of the plasma pressure, they can produce repetitive energy losses to the wall through magnetic modulation. The peak values of the particle and the heat fluxes increased by 10% with magnetic modulation compared with those in the steady state. We clearly observed that magnetic modulation leads to periodic particle and energy release/loss to the wall, similar to ELM-like phenomena.

From the heat flux perpendicular to the wall and the ELM energy loss caused by a single ELM, we can determine the values of the magnetic energy density variation by

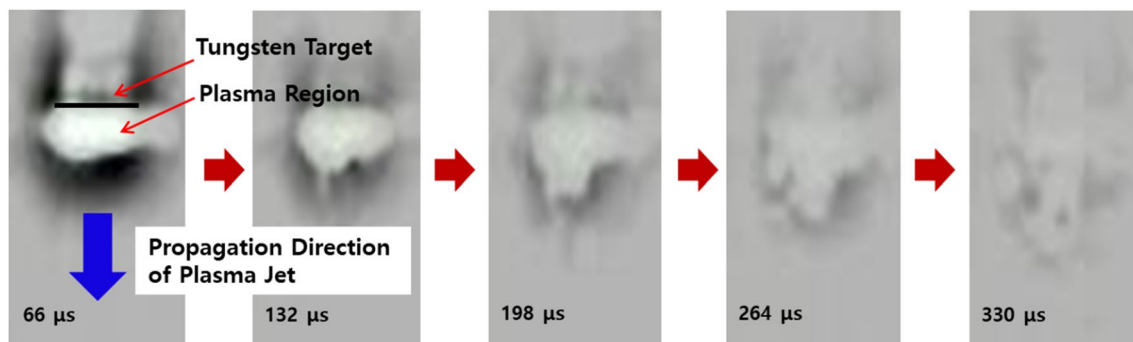


Fig. 18 Fast camera images for dusty plasma propagation generated by laser irradiation on the tungsten target

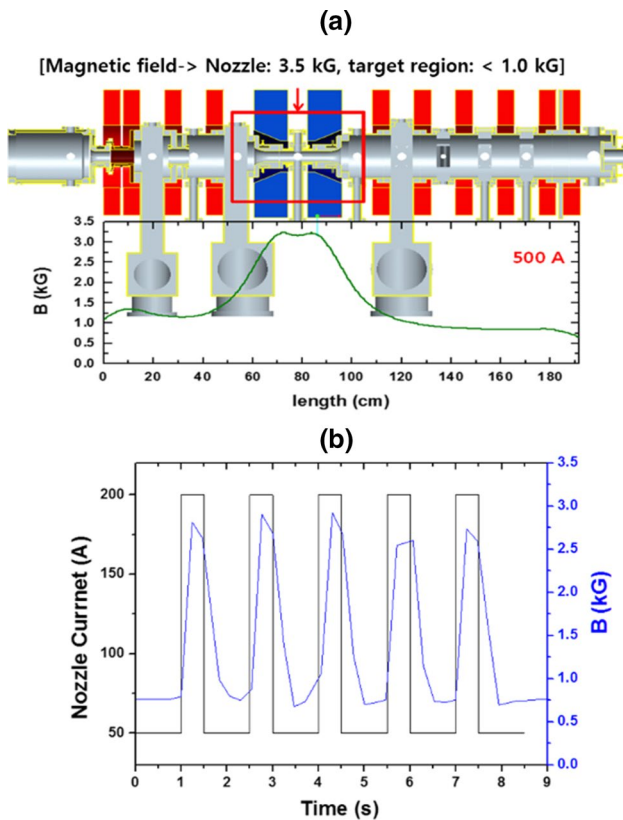


Fig. 19 Modulated magnetic field by changing the current in the nozzle magnets located near the axial center of the DiPS-2

calculating the magnetic modulation (ΔE_B ; $B = 1\text{--}2.8$ kG, $\Delta B \sim 65\%$, duration = 0.5 s) as $E_B = B^2/2\mu_0$, and the theoretical ratio of generated energy is $E_{B1}/E_{B0} \sim 12.3\%$, where $B_0 = 2.8$ kG and $B_1 = 1.0$ kG, as shown in Fig. 21. Considering that W_{B1}/W_{B0} is the energy loss to the wall by modulation, it can be compared with the experimental results. The plasma energy at the edge region (E_{edge}) near the wall is calculated as $E_{\text{edge}} \sim nT_e (T_i \ll T_e)$ from the probe measurements. The ratio of the energy released due to magnetic modulation is $E_{\text{edge},B1}/E_{\text{edge},B0} \sim 1.67\%$. The total plasma energy in the DiPS-2 (W_p) can be written as $W_p = \frac{3}{2}n(T_e + T_i)V_p$, ~ 80 mJ, ($T_i \ll T_e$), and the rate of energy loss to the wall from the total plasma energy resulting from transient heat flux in the DiPS-2 is $W_{\text{wall}}/W_p \sim 0.75\%$. As shown in Table 2, these experimental results are much smaller than the theoretical value, which may occur because the end loss is much larger than the loss to the wall in a linear device. During ELMs in tokamaks, the energy loss per ELM is related to the input power as $(f_{\text{ELM}} \times \Delta W_{\text{ELM}})/P_{\text{input}} = \text{constant}$. As a result of the low input power and frequency, an energy loss smaller than the theoretical value and that in the KSTAR case may be possible. Furthermore, an experimental evaluation of the ELM energy loss to the wall in KSTAR was conducted in a previous experiment [25]. The energy loss

rate resulting from the transient heat flux in DiPS-2 is comparable to that of the KSTAR ($W_{\text{wall,ELM}}/W_{\text{tot}} \sim 0.5\%$). The energy loss rate and ELM velocities in tokamaks and the DiPS-2 are listed in Table 2.

5 Summary

As a part of the Basic Fusion Research of the Korean Fusion Program, the Fusion Core Research Center (FCRC) program has been an important resource for training young researchers and developing diagnostics and physics for the KSTAR and the ITER devices. Hanyang University has been a part of the FCRC program for the past 10 years, or so. We summarize research regarding simulations of fusion edge plasmas using linear plasma devices in terms of physics and plasma–material interactions conducted in the following programs: Center for Edge Plasma Science (cEps), Dust interaction of Plasmas with Surfaces (DiPS), and Center for interactions of Materials with Plasmas (cimpL).

To simulate both the edge plasmas and ELM phenomena of toroidal devices, we performed experiments exposing the wall in the DiPS-2, which has edge-relevant physical parameters (steady-state magnetic field up to 1 kG, $n_e \sim 10^{19} \text{ m}^{-3}$, $T_e = 1\text{--}15$ eV) and geometry (radius of chamber = 102 mm, radius of magnetic nozzle = 25.2 mm, length = 2526 mm), to a transient heat flux. An LaB₆ cathode consisting of a disk with a 4 inch diameter and 1/4 inch thickness was used in the DiPS-2; it was indirectly heated using a graphite heater. The plasma was produced with greater than a 5 kW (280 A, 18 V) heating power and 3–20 kW (30–100 A, 100–200 V) discharge power with argon, helium, and hydrogen. The DiPS-2 has a magnetic nozzle to apply a stronger magnetic field in the middle of the device with a nozzle-shaped structure, which generates a simulated magnetized SOL region in the fusion device.

The ELM phenomena were simulated using a magnetic modulation in the DiPS-2. The transient heat and the particle fluxes on the wall were compared with those of the KSTAR device. Periodic particle and energy released/lost to the wall, similar to ELM-like phenomena, were observed with magnetic modulation. Steady-state plasma parameters were measured at the wall with fixed electric probes, and they are compared to those for transient conditions. An approximately 10% increase in particle and heat fluxes compared with those in the steady state was measured at the wall during modulation. The energy loss rate resulting from the transient heat flux in the DiPS-2 ($\sim 0.75\%$) was found to be comparable to that of KSTAR ($\sim 0.5\%$). As a linear machine, the measured energy and particle losses to the radial wall seemed to be much less than the theoretical value because of the losses to the end plate.

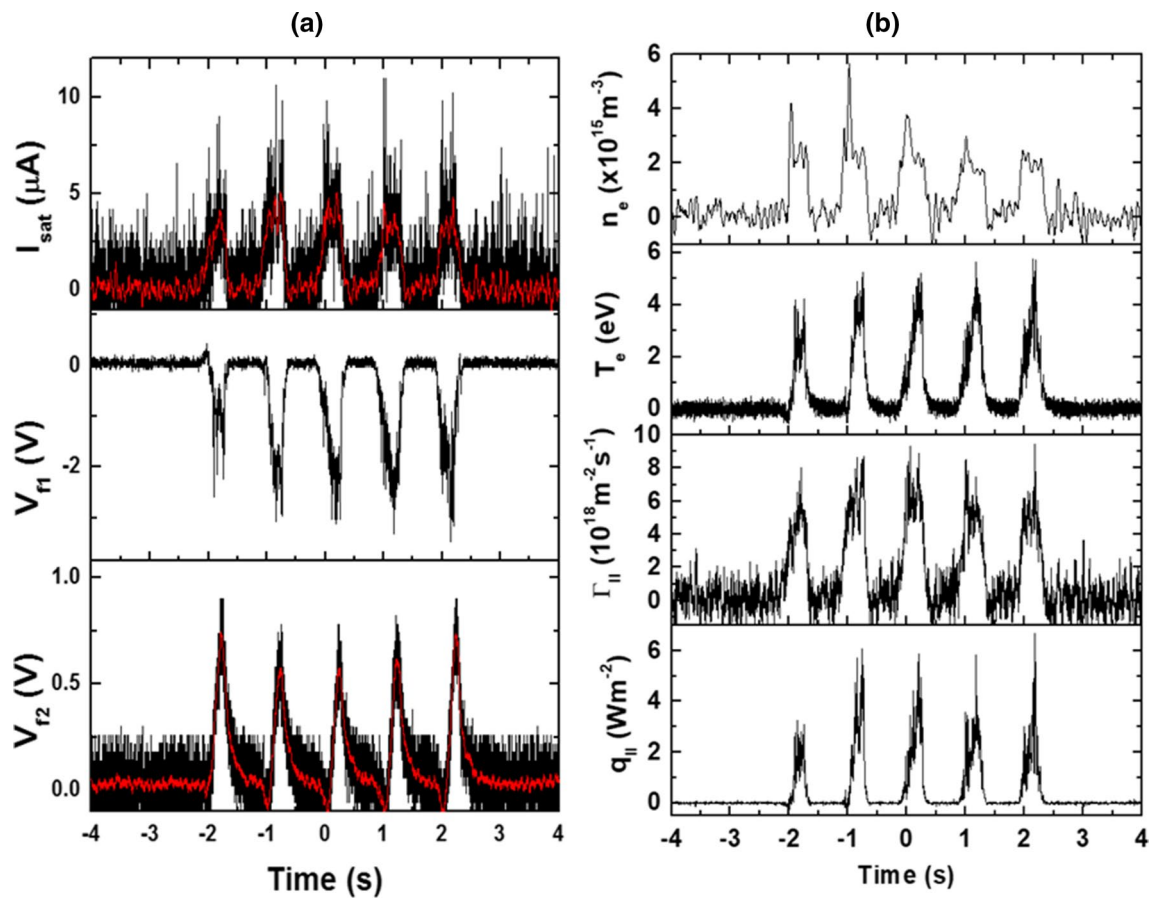


Fig. 20 Triple probe measurements: **a** raw data and **b** calculated plasma parameters during magnetic modulation in the DiPS-2

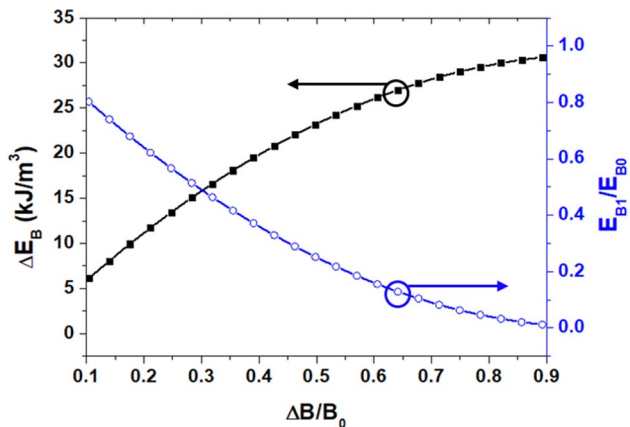


Fig. 21 Magnetic energy density variation (ΔE_B , solid black squares) and ratio of generated energy (E_{B1}/E_{B0} , open blue circles) caused by magnetic modulation

ELMs were also experimentally simulated using the interaction of a high-energy pulsed laser with tungsten targets in a magnetized plasma in the DiPS-2. Under steady-state and transient conditions, the characteristics of the plasma

Table 2 Energy loss rate and ELM velocities in tokamaks and the DiPS-2

	$\frac{\Delta W_{\text{ELM}}}{W_{\text{tot}}}$	$\frac{W_{\text{wall}}}{W_{\text{tot}}}$	V_r [km s^{-1}]	V_t [km s^{-1}]	Ref.
JET	4.5	0.4	0.1–0.7		[47]
AUG	3		0.5	15	[48, 49]
JT60U	5		0.4–1.5	20–30	[50]
DIII-D	2–6		0.33–2.6		[51]
KSTAR	2	0.5	0.1–0.3	11	[25]
DiPS-2	1.67	0.75	0.1–0.5	0.1	

density in magnetized plasmas were estimated to determine the effects of dusty plasma injection on the plasma parameters. The transient energy flux of the pulsed laser was $\sim 100 \text{ MJ m}^{-2} \text{ s}^{-1/2}$ per laser shot, and the beam injection frequency was fixed at 20 Hz because type-I ELMs in fusion devices occur at frequencies of approximately 10–200 Hz. When the ELM-like condition was replicated by exposing a tungsten surface to a pulsed laser beam, the effects of dusty plasma injection on the plasma density of an edge-relevant plasma were highly dependent on n_e .

A free presheath, in contrast to a bounded presheath, was produced in a magnetized plasma by inserting a TPO into the plasma stream in the DiPS-2 for experimental simulation of the transport phenomena at the edges of fusion toroidal plasmas. The plasma parameters at the ram of the TPO and those at the wake showed clear differences from those of normal operating plasmas without a TPO. On the basis of these measurements at the back side of the TPO, D_{\perp} and L_c were investigated. The tendency of D_{\perp} results was satisfied when D_B varied according to T_e/B , and an L of ~ 10 cm was obtained for the free presheath.

Heat loads deposited on the first wall due to mitigated type-I ELMs are expected to be the dominant contributor to the total thermal plasma wall load of the ITER, particularly in the upper main chamber during the baseline H-mode magnetic equilibrium because of the fast radial convective heat propagation of the ELM filaments before complete loss to the divertor. The radial dependence of the peak filament heat flux parallel to the wall was observed to be exponential, with a decay length of $\lambda_{q,ELM} \sim 25 \pm 4$ mm and a heat flux of $q_{\parallel,ELM} = 0.05$ MW m $^{-2}$ at the wall, corresponding to $q_{\parallel} \sim 7.5$ MW m $^{-2}$ at the second separatrix.

Carborane (C $_2$ B $_{10}$ H $_{12}$), a non-toxic boron-containing material, has been used to deposit amorphous hydrogenated carbon/boron (a-C/B:H) thin films using a helium DC glow discharge. Because the deposition mechanism is dominated by low-energy ions, radicals, and neutrals, the films are not affected by the position inside the vacuum chamber or the duty cycle. In particular, the thin films deposited inside KSTAR were characterized using variable angle spectroscopic ellipsometry, XPS, and AES. The carbon flux on the wall was found to be approximately 1.78×10^{16} cm $^{-2}$ s $^{-1}$ using a cavity technique.

A carbon/graphite tile was irradiated with a helium plasma with a high flux and low energy in the DiPS-2. Changes in the surface morphology were observed using SEM. The electrical conductivity was decreased by observing the four-probe measurements, and the intensity of the graphite disorder peak was also increased using the results of Raman spectroscopy.

Nitrogen gas was injected at a rate of 2.5–30% as an impurity into a helium plasma in the DiPS-2 with a LaB $_6$ cathode. With nitrogen injection, the plasma parameters decreased as the density by 60%, and the electron temperature by 20% along with the gradual decrease of heat flux.

We investigated the irradiation effects of a low-energy helium plasma on a graphite tile, the first-wall material of KSTAR, under the condition of high flux. Surface erosion caused by the RES was observed. The intensity of the D peak, indicating an induced structural disorder, was markedly increased. The electrical conductivity decreased from 520 to 220 Ω^{-1} cm $^{-1}$ because of a combination of morphological degradation and induced structural disorder.

To develop efficient lithium injection, the density profiles of lithium vapor of the LIGHT-1 device were analyzed, and a lithium injector for the LHD was tested. The radial and axial variations in the densities of lithium neutrals and ions were analytically calculated for a cylindrical chamber by assuming classical diffusion with or without a magnetic field. Proper combinations of the relaxation length and size of the source produced well-fitted profiles similar to those observed experimentally and those obtained using Monte Carlo codes.

A tungsten damage test was conducted in the DiPS-2 using ELM simulations with laser irradiation. The heat load was approximately 1–10 MW m $^{-2}$, similar to the steady-state plasmas of the ITER divertor. An Nd:YAG pulsed laser was used as a source of transient heat load (~ 100 MJ m $^{-2}$ s $^{-1/2}$ per laser shot), like the ELMs on tungsten targets in a plasma. After irradiation of the tungsten targets in plasma using a pulsed laser, micro-sized cracks, melt layers, and the recrystallization of tungsten targets, which appeared to have a striped pattern on a nanoscale, were observed.

The generation of tungsten dust was experimentally investigated by exposing tungsten targets to irradiation by a high-energy pulsed laser with a transient heat flux factor. The rate of dust generation was observed to increase linearly with respect to F_{HF} . An approximate estimate of dust generation, obtained using the area ratio between the beam irradiation and the ITER chamber, was obtained.

Acknowledgements This research was supported by the National R&D Program through the National Research Foundation of Korea (NRF) funded by the Ministry of Science, ICT and Future Planning (2019M1A7A1A03088471). This research was partially supported by R&D Program of “Plasma Convergence and Fundamental Research (1711124796)” through the Korea Institute of Fusion Energy (KFE) funded by the Government funds, Republic of Korea.

References

1. G. Federici et al., Nucl. Fusion **41**, 1967 (2001)
2. N. Asakura et al., Nucl. Fusion **44**, 503 (2004)
3. B. Lipschultz, D. Whyte, B. LaBombard, Plasma Phys. Control. Fusion **47**, 1559 (2005)
4. N. Smick, B. LaBombard, C. Pitcher, J. Nucl. Mater. **337–339**, 281 (2005)
5. J.P. Coad et al., Nucl. Fusion **46**, 350 (2006)
6. R.A. Pitts et al., Plasma Phys. Control. Fusion. **47**, B303 (2005)
7. B. Lipschultz et al., Nucl. Fusion **41**, 585 (2001)
8. J. Winter, Plasma Phys. Control. Fusion **46**, B583 (2004)
9. C. Voinier, C.H. Skinner, A.L. Roquemore, J. Nucl. Mater. **346**, 266 (2005)
10. F. L. Guern, et al., R&D on in-vessel dust and tritium management in ITER. in 2011 IEEE/NPSS 24th symposium on fusion engineering **SP1–24**, 1–5 (2011)
11. R.A. Causey, J. Nucl. Mater. **300**, 91 (2002)
12. D.M. Goebel, Y. Hirooka, T.A. Sketchley, Rev. Sci. Instrum. **56**, 1717 (1985)
13. Y. Hirooka et al., J. Vac. Sci. Technol. A **8**, 1790 (1990)

14. N. Ohno et al., Nucl. Fusion **41**, 1055 (2001)
15. A. Kreter, Fusion Sci. Technol. **68**, 8 (2015)
16. G.D. Temmerman et al., Fusion Eng. Des. **88**, 483 (2013)
17. J. Rapp, et al., Nucl. Fusion **57** (2017)
18. H. Liu et al., Fusion Eng. Des. **144**, 81 (2019)
19. K.-S. Chung et al., Fusion Sci. Technol. **63**, 16 (2013)
20. I.J. Kang et al., Curr. Appl. Phys. **17**, 358 (2017)
21. I.J. Kang et al., Plasma Sci. Technol. **22**, 045601 (2020)
22. R.A. Pitts et al., J. Nucl. Mater. **415**, S957 (2011)
23. K.-S. Chung, J. Korean Phys. Soc. **33**, 54 (1998)
24. P.C. Stangeby, *The plasma boundary of magnetic fusion devices* (IOP Publishing Ltd, Bristol, 2000)
25. M.-K. Bae et al., Nucl. Mater. Energy **12**, 1259 (2017)
26. J.G. Bak et al., Contrib. Plasma Phys. **53**, 69 (2013)
27. H.-S. Kim et al., Fusion Eng. Des. **109–111**, 809 (2016)
28. J.-H. Sun et al., J. Phys. Soc. **62**, 612 (2013)
29. S.-H. Hong et al., J. Nucl. Mater. **415**, S1050 (2011)
30. H.S. Kim et al., J. Kor. Phys. Soci. **61**, 832 (2012)
31. I.S. Park et al., Sci. Adv. Mater. **13**, 2270 (2021)
32. K.-S. Chung et al., Fusion Eng. Des. **119**, 61 (2017)
33. H. Tsuchiya et al., Fusion Eng. Des. **85**, 847 (2010)
34. S. Ciattaglia, Dust inventory control status in ITER Baseline provisions, R&D plan and first results, in 2nd RCM of IAEA Dust CRP (2010)
35. J.W. Connor, Plasma Phys. Control. Fusion **40**, 531 (1998)
36. K.-S. Chung et al., Contrib. Plasma Phys. **46**, 354 (2006)
37. R.P. Doerner et al., J. Nucl. Mater. **290**, 166 (2001)
38. I.J. Kang et al., JINST **10**, C12019 (2015)
39. M. Shoji et al., Plasma Phys. Control. Fusion **43**, 761 (2001)
40. J.W. Coenen et al., J. Nucl. Mater. **415**, S78 (2011)
41. G. Pintsuk et al., Fusion Eng. Des. **82**, 1720 (2007)
42. J.W. Coenen et al., Nucl. Fusion **51**, 083008 (2011)
43. A. Huber et al., Phys. Scr. **T159**, 014005 (2014)
44. R.A. Pitts et al., Nucl. Mater. Energy **12**, 60 (2017)
45. R.A. Pitts et al., Nucl. Mater. Energy **20**, 100696 (2019)
46. A.W. Leonard et al., J. Nucl. Mater. **266–269**, 109 (1999)
47. R.A. Pitts et al., J. Nucl. Mater. **390–391**, 755 (2009)
48. G.S. Yun et al., Phys. Rev. Lett. **107**, 045004 (2011)
49. A. Kirk et al., Plasma Phys. Control. Fusion **53**, 035003 (2011)
50. N. Asakura et al., J. Phys. Conf. Ser. **123**, 012009 (2008)
51. X.Q. Xu et al., Phys. Plasma **10**, 1773 (2003)

Publisher's Note Springer Nature remains neutral with regard to jurisdictional claims in published maps and institutional affiliations.

Authors and Affiliations

In Je Kang^{1,2} · Min-Keun Bae¹ · In Sun Park¹ · Hyun-Jong Woo³ · Taihyeop Lho² · Jeong-Sun Ahn¹ · Doo-Hee Chang¹ · Soon-Gook Cho¹ · Geun-Sik Choi¹ · Heung-Gyun Choi¹ · Yong-Sup Choi¹ · Bo-Hyun Chung¹ · Tae Hun Chung⁴ · Jeong-Joon Do¹ · Bon-Cheol Goo¹ · Sung Hoon Hong¹ · Suk-Ho Hong⁵ · Jong-Sik Jeon¹ · Sung-Kiu Joo¹ · Seo Jin Jung¹ · Seok-Won Jung¹ · Young-Dae Jung⁶ · Yong Ho Jung¹ · Kwang-Cheol Ko⁷ · Beom-Sik Kim¹ · Gon-Ho Kim⁸ · Hye-Ran Kim¹ · Heung-Su Kim⁵ · Jin-Hee Kim¹ · Jong-Il Kim¹ · Jae Yong Kim⁹ · Kyung-Cheol Kim¹ · Myung Kyu Kim¹ · Sang-You Kim¹ · Jin-Woo Kim¹ · Yong-Kyun Kim¹⁰ · Gyea Young Kwak¹ · Dong-Han Lee¹ · Heon-Ju Lee¹¹ · Min Ji Lee¹ · Myoung-Jae Lee⁹ · Seung-Hwa Lee¹ · Eun-Kyung Park¹ · Dong Chan Seok¹ · Byoung-Kyu Lee¹ · Seung Jeong Noh¹² · Young-Jun Seo¹ · Yun-Keun Shim¹ · Jong Ho Sun¹ · Byung-Hoon Oh¹ · Cha-Hwan Oh⁸ · Hye Taek Oh¹ · Young-Suk Oh¹ · Sang Joon Park¹ · Hyun Jong You¹ · Hun Suk You¹ · Kyu-Sun Chung¹

¹ Applied Plasma Laboratory, Department of Electrical Engineering, Hanyang University, Seoul 04763, Korea

² Institute of Plasma Technology, Korea Institute of Fusion Energy, Gunsan 54004, Korea

³ Agency for Defense Development, Daejeon 34186, Korea

⁴ Department of Physics, Dong-A University, Busan 49315, Korea

⁵ Korea Institute of Fusion Energy, Daejeon 34133, Korea

⁶ Department of Applied Physics, Hanyang University, Ansan 15588, Korea

⁷ Department of Electrical Engineering, Hanyang University, Seoul 04763, Korea

⁸ Department of Energy Systems Engineering, Seoul National University, Seoul 08826, Korea

⁹ Department of Physics, Hanyang University, Seoul 04763, Korea

¹⁰ Department of Nuclear Engineering, Hanyang University, Seoul 04763, Korea

¹¹ Department of Energy Engineering, Jeju National University, Jeju 63243, Korea

¹² Department of Applied Physics, Dankook University, Yongin 16890, Korea